Selenium Inclusion in $Cu_2ZnSn(S,Se)_4$ Solar Cell Absorber Precursors for Optimized Grain Growth

Nils Ross ⓘ, Sigbjorn Grini, Katharina Rudisch, Lasse Vines, and Charlotte Platzer-Björkman

Abstract—**$Cu_2ZnSn(S,Se)_4$ precursors are fabricated by compound cosputtering from metal sulfide and selenide targets, and annealed in mixed argon, sulfur, and selenium atmosphere at temperatures between 540 and 580 °C and at pressures between 24 and 47 kPa. We produce solar cell devices from these absorbers that range from 2.0% to 9.0% power conversion efficiency. We extensively characterize the morphology and elemental composition of the absorbers, and are able to closely relate the annealing conditions, precursor sulfur–selenium content, device performance, and absorber quality. We develop a qualitative model which relates the sulfur–selenium distribution in the precursor and the relative partial pressures of sulfur and selenium during the annealing process to the absorber properties. We show that selenium inclusion in the precursor allows more rapid recrystallization of the absorber at lower temperature. Alternating stacking of sulfur and selenium containing precursor material leads to differential rates of recrystallization, which allows some control over the morphology of the annealed absorber and Zn(S,Se) secondary phase segregation in that absorber. We further show that selenium containing precursors can be used to fabricate the superior devices relative to sulfur-only precursors, when the annealing phase space is subject to severe practical restrictions.**

Index Terms—**Annealing, CZTSSe, sulfoselenization, Zn(S,Se).**

I. Introduction

TO DATE, the most successful means of fabricating the $Cu_2ZnSn(S,Se)_4$ (CZTSSe) absorber layer in CZTSSe solar cells involves a multistep process. A thin-film precursor material containing the cations and in some cases chalcogen atoms is deposited in the first step, then subjected to single or series of thermal annealing steps in a chalcogen atmosphere.

The record-holding, 12.6% power conversion efficiency (PCE) device and related high-performance devices from IBM were formed by depositing sulfur and selenium containing CZTSSe precursors from a hydrazine pure-solution or slurry [1]–[3] and annealing at 540 °C in a sulfur-rich atmosphere. Hydrazine is toxic and difficult to handle, and an alternative dimethyl sulfoxide solution process, which yields a selenium-free precursor, has produced 11.2% efficient solar cells from a three-stage annealing process [4].

Vacuum-processed precursors can also be produced: the current record for vacuum-processed CZTSSe is 12.3%, with an absorber formed from a sputtered stacked metal precursor, annealed in the presence of Se and SeS_2 [5]. Sputtering is a highly scalable, high-throughput method of thin film deposition which is well established in industry. It is well suited to inline scale up in conjunction with the vacuum-annealing required to produce recrystallized CZTSSe absorbers. It also offers the flexibility of precursor production via a range of methods, including metal stacking [5], metal cosputtering [6], reactive cosputtering [7], and compound cosputtering [8].

Despite the fact that the current record CZTSSe device was fabricated from a precursor containing both selenium and sulfur, extant studies of sputtered precursors largely concern metallic or metal sulfide precursors. The interaction of quaternary compound-target sputtered $Cu_2ZnSnSe_4$ (CZTSe) precursor with a sulfur atmosphere during annealing has been explored with regard to experimentally accessible [S]/([S] + [Se]) ratios [9]. However, the absorber material was not used to fabricate solar cells or characterized by photoluminescence, so its quality for solar cell applications is difficult to assess. Postsulfurization of annealed CZTSSe absorbers [5], [10] has proven to be an effective method of reducing the open-circuit voltage deficit, but the effect on device performance of selenium inclusion in the precursor is less thoroughly investigated in the literature.

In this study, we fabricate CZTSSe-absorber solar cells from compound cosputtered selenium containing precursors using a two step process. We utilize $CuZnSnS_4$ (CZTS) and $CuZnSnSe_4$ precursors, as well as bilayer stacked combinations of the two materials. We anneal these precursors in the presence of both elemental sulfur and selenium, in a background argon atmosphere, and in doing so produce solar cell absorber material with a sulfur-to-total-chalcogen ratio $S_r = [S]/([S]+[Se]) \simeq 0.4$. Inclusion of sulfur in the annealing atmosphere limits the thickness of $Mo(S,Se)_2$ formation at the back contact, and ensures that the S_r value of the absorber is only weakly dependent on the precursor chalcogen composition, as we will show in this

TABLE I
PRECURSOR PROPERTIES - XRF

Precursor	Material	[Cu]/[Sn]	[Zn]/([Cu]+[Sn])	[Cu]/([Zn]+[Sn])	[Zn]/[Sn]
B	CZTS	1.91±0.02	0.35±0.01	0.95±0.02	1.02±0.02
C	CZTSe	1.88±0.02	0.37±0.01	0.91±0.02	1.07±0.02
F	CZTSe-atop-CZTS	1.91±0.02	0.36±0.01	0.93±0.02	1.05±0.02
Ff	CZTSe-atop-CZTS	1.86±0.02	0.36±0.01	0.92±0.02	1.03±0.02
G	CZTS-atop-CZTSe	1.91±0.02	0.36±0.01	0.93±0.02	1.05±0.02

study. We aim to assess the impact of selenium inclusion on absorber growth during annealing, and of the mixed chalcogen atmosphere and precursors on the quality of solar cells so fabricated. In parallel, we optimize the annealing conditions with a survey of argon background pressure and annealing temperature, and show that the precursor chalcogen engineering can be used to compensate for some of the practical limitations of our annealing apparatus.

II. EXPERIMENTAL DETAILS

Bilayer molybdenum back contacts were sputtered onto soda-lime glass substrates. Cu$_2$ZnSn(S/Se)$_4$ precursor material was cosputtered using a Lesker CMS-18 sputter system in an Ar atmosphere from chalcogen-compound targets CuS, CuSe, SnS, SnSe, ZnS, and ZnSe. Sulfur and selenium content of the precursors could be varied by sputtering from sulfide or selenide targets. For ease of sputter process calibration, precursor layers were sputtered as either complete sulfide or complete selenide. Mixed sulfoselenides were sputtered as tests but did not produce distinct behaviors, and have not been included in this paper. No extra sodium source beyond the SLG was added.

Five precursors (B, C, F, Ff, and G) were sputtered, each approximately 1200 nm thick. Precursor properties are listed in Table I. Precursors B and C were single layers of CZTS and CZTSe precursor, respectively. Precursors F and Ff, hereafter referred to as F(f), were bilayers, with a ~500-nm bottom layer of CZTS and ~700-nm top layer of CZTSe. Some samples from precursor F were used for investigation of the behavior of the chalcogen step during the annealing process, and could not be made into devices. Precursor Ff was fabricated to provide replacement precursor material: its cation content was slightly different, but we show in the device results that it produced similar quality absorbers (see Fig. 8). Precursor G had the reverse orientation to F, with a 700-nm CZTSe underlayer and a 500-nm CZTS overlayer. Thus, precursors F(f) and G constitute a set of samples for exploring the impact of precursor sulfur–selenium distribution on annealed absorber properties.

In Table I, we list the precursor properties and cation ratios. We express the cation ratios by both [Cu]/[Sn] and Zn/([Cu]+[Sn]) and [Zn]/[Sn] and [Cu]/([Zn]+[Sn]). The precursors had overall [Cu]/[Sn] ratios 1.85–1.92(±0.02) and [Zn]/([Cu] + [Sn]) ratios of 0.35–0.37(±0.01), as determined by Rutherford backscattering-calibrated X-ray fluorescence measurements. That is, our precursors are slightly zinc rich and copper poor. The morphology of the precursors is columnar, as can be seen later in Fig. 7, or for similar samples in [11]. These

TABLE II
DEVICE OPTIMIZATION ANNEALS

Anneal #	P [kPa]	T [°C]	time [min.]
6	24	540-560	3
7	24	550-570	3
8	24	560-580	3
9	47	560-580	3
10	35	550-570	3
11	35	560-580	3
12	35	560-580	4

precursors are structurally similar to those formed by reactive sputtering of metal targets under H$_2$S-rich conditions, and have a zinc-blende structure [12].

Samples were annealed in a tube furnace in a pyrolytic carbon-coated graphite box containing solid masses of 5-mg elemental sulfur and 50-mg elemental selenium. Annealing temperatures were between 540 and 580 °C. Samples were ramped rapidly to high temperature by transfer from a cold zone to a hot zone within the furnace: ramp time between room temperature and starting annealing temperature was 80–90 s. Argon pressures were 24, 35, and 47 kPa. Most anneals were for 3 min, with an internal ramp time between the lower and upper bound annealing temperatures of approximately 90 s. The graphite box has a 1-mm-diameter hole in the top to facilitate pump down. When the box is pushed into the hot zone of the furnace, the block closes over this hole. However, we have previously reported sulfur loss for annealing times longer than 3 min [13], indicating that this seal is not complete. Most of the anneals are therefore not more than 3 min long. Anneal 12 was 4 min long to check for sample degradation due to excessive sulfur loss. At the end of the anneal, samples were quenched by transfer from the hot zone to the cold zone of the furnace, with cooling to 150 °C over 300 s. Excess chalcogen containing Ar atmosphere was pumped away at 150 °C. Table II summarizes the anneal conditions.

Our reported anneals begin at number "6" because we performed an initial survey of six different annealing conditions, with varying elemental sulfur–selenium mass ratios and background pressures [14]. The sixth condition, with 5 mg of sulfur and 50 mg of selenium, 27 kPa, and 560 °C, produced devices of up to 7.3% PCE without air annealing and was chosen as the basis for this device optimization series. The results of this initial survey are not included here for brevity, but it is worth noting that failure to include a sulfur source in the anneal led to extremely thick MoSe$_2$ layers in CZTSe precursors. Failure

to include a selenium source led to annealed CZTS absorbers with less than 3% selenium content. We complete the optimization in this paper by varying temperature and pressure, and by air-annealing the recrystallized absorbers prior to device fabrication. Note that we have placed the highest pressure anneal "9" in the middle of the series, not the end, so that the more similar annealing conditions of 6–8 and 10–12, respectively, are separated on our graphs and thus not as visually confusing.

Absorbers were air annealed following chalcogen annealing, face-up on a hot plate in clean-room ambient atmosphere, at a temperature of 300 °C, for 10 min. These were the optimum air anneal conditions from an earlier study of CZTS precursors annealed in elemental selenium and having absorber $S_r \simeq 0.2$ [15]. We tested these conditions with a number of CZTS precursors, and found that the 300 °C, 10 min condition produced close to optimum device results. Solar cell devices were fabricated from the air annealed absorbers. The absorber was etched in KCN, followed by chemical bath deposition of a 60-nm CdS layer. A window layer of i-ZnO (80 nm)/Al:ZnO (210 nm) was deposited by sputtering. The devices were finished by evaporation of Ni/Al/Ni front contacts and mechanical scribing to define 0.5 cm^2 cells.

Absorbers were characterized by grazing incidence X-ray diffraction (GIXRD) in a Siemens D5000 diffractometer. For annealed absorbers, S_r could be estimated by assuming a linear shift of the 112 peak between CZTSe (27.16° [JCPDS 04-010-6295]) and CZTS (28.44° [JCPDS 04-005-0388]) with increasing sulfur percentage: $S_r = (x - 27.16)/1.28$, for x the 112 peak position. We made no assumptions concerning the secondary phase composition from GIXRD, due to the well-known overlap of the ZnS and ZnSe peaks with the CZTSSe peaks [16]. We have characterized the Zn(S,Se) secondary phase using Raman spectroscopy. Raman spectroscopy was performed using a Renishaw Invia equipped with both 532-nm and 325-nm lasers.

Scanning electron microscope (SEM) images and energy dispersive X-ray spectroscopy (EDX) line scans were obtained with a Zeiss Merlin device. Acceleration voltage was 5–7 kV to minimize the interaction volume for cross-sectional analysis and interaction volume diameter has been estimated by Monte Carlo simulation to be 170–200 nm. Lines analyzed were Cu-L, S-K, Se-L, Zn-L, and Sn-L. The Cu-L and Zn-L overlap was deconvolved using Oxford Instruments' AZtec software. The Mo-L line overlaps the S-K line heavily and was not deconvolved.

Secondary ion mass spectrometry (SIMS) depth profile measurements were performed using a Cameca IMS 7f instrument with a primary beam of 5-keV Cs$^+$ ions. The beam was scanned across a raster of 150 μm × 150 μm, where a central region with a diameter of 33 μm was used for analysis. In order to minimize the potential matrix effects due to a change in S_r, MCs$^+$ clusters were detected in SIMS, where "M" is the element to be analyzed [17]. ^{63}Cu, ^{64}Zn, and ^{120}Sn are presented normalized to their maximum intensities and scaled for clarity. ^{23}Na, ^{32}S, and ^{80}Se were normalized by the maximum ^{98}Mo intensity.

Current–voltage measurements (IV) were performed in a one-sun solar simulator (Newport, ABA). Quantum efficiency (QE) measurements were performed under dark conditions, in a home-made setup calibrated by externally measured Hama-
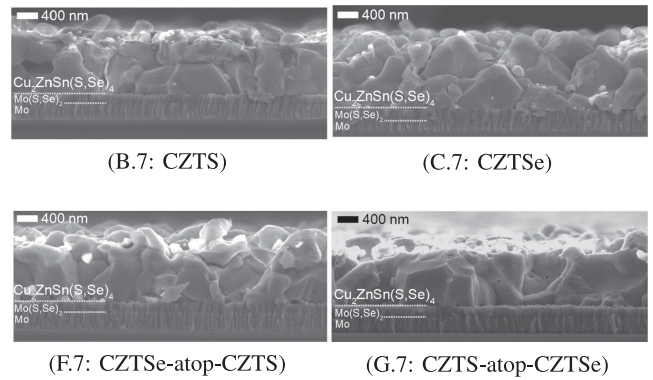

Fig. 1.   Cross-sectional SEM for Anneal 7: 24 kPa, 550–570 °C, 3 min. Precursor chalcogen layers are shown beside the sample labels. Small bright contrast particles were confirmed to be Zn(S,Se) by EDX.
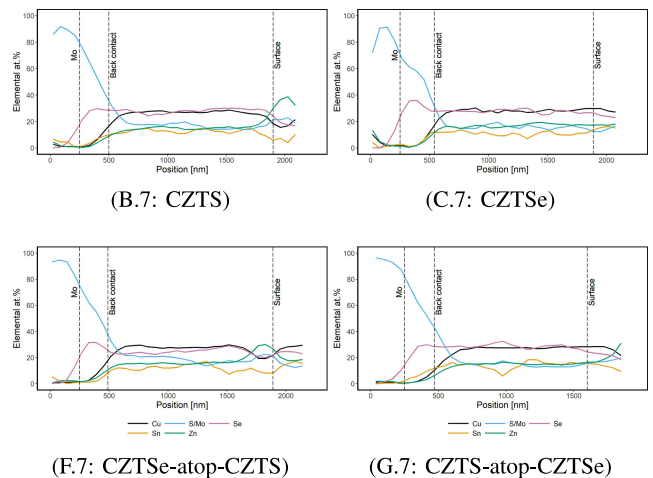

Fig. 2.   Example EDX line scans for Anneal 7: 24 kPa, 550–570 °C, 3 min. The Sn-L line is very close to the energy cutoff, with a consequently noisy signal, and should not be overinterpreted. Regions of increased Zn and S intensity correspond to Zn(S,Se) grains.

matsu Si and InGaAs solar cells. Reflectivity measurements were made using a Bentham PVE300 photovoltaic characterization system, with diffuse reflections collected via integrating sphere.

III. RESULTS

Cross-sectional SEM and EDX scans were performed for this series of samples after air annealing and prior to surface etching by KCN. A selection of cross-sectional SEM images are shown in Fig. 1 for anneal 7. Representative EDX line scans from anneal 7 are shown in Fig. 2. Bright contrast particles in the SEM images corresponded in EDX to regions of high Zn and S concentration and lowered Cu, Sn, and Se concentration. These particles are therefore interpreted to be Zn(S,Se) grains, which are more sulfur-rich than the surrounding absorber. No selenium-only ZnSe grains were resolved in any of the EDX data.

Sulfur–selenium steps in the precursor were removed after annealing, and replaced by essentially depth-uniform sulfur–selenium ratios. No sulfur–selenium gradient remained in any
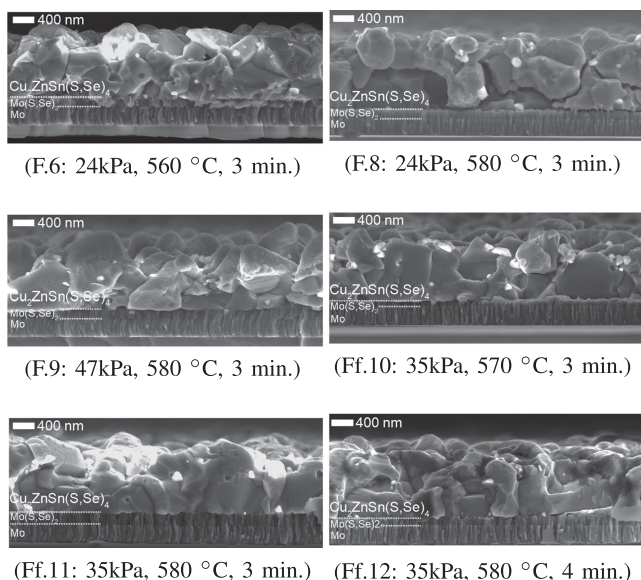
(F.6: 24kPa, 560 °C, 3 min.) (F.8: 24kPa, 580 °C, 3 min.)

(F.9: 47kPa, 580 °C, 3 min.) (Ff.10: 35kPa, 570 °C, 3 min.)

(Ff.11: 35kPa, 580 °C, 3 min.) (Ff.12: 35kPa, 580 °C, 4 min.)

Fig. 3. Cross-sectional SEM of all precursors for bilayer Precursor F: CZTS bottom layer, CZTSe top layer. Small bright contrast particles were confirmed to be Zn(S,Se) by EDX.

(G.6: 24kPa, 560 °C, 3 min.) (G.8: 24kPa, 580 °C, 3 min.)

(G.9: 47kPa, 580 °C, 3 min.) (G.10: 35kPa, 570 °C, 3 min.)

(G.11: 35kPa, 580 °C, 3 min.) (G.12: 35kPa, 580 °C, 4 min.)

Fig. 4. Cross-sectional SEM of all precursors for bilayer Precursor G: CZTSe bottom layer, CZTS top layer. Small bright contrast particles were confirmed to be Zn(S,Se) by EDX.

of precursor G's anneals. Some front-to-back variation in S_r was present in most anneals for precursors F(f), with the back being slightly sulfur-rich. However, this variation was always small, with a $\Delta S_r \leq 0.1$, and as in Fig. 2, the sulfur–selenium gradients were not always smooth. Abrupt changes in sulfur–selenium ratio result from neighboring grains with differing S_r, rather than from smooth variation of sulfur–selenium ratio within grains.

The primary difference between precursors for a given set of annealing conditions is the resulting morphology and distribution of the Zn(S,Se) secondary phase. These differences are highlighted in Fig. 1, showing precursors B-G after anneal 7 and the air anneal, but prior to KCN etching. Referring to the CZTSSe phase itself, CZTS-surface precursor G in particular is more flat after annealing than CZTSe-surface precursors C and F, which have more rough surfaces. CZTSe containing precursors C and G have the largest and most uniform grain size, with grains that generally reach from the Mo/Mo(S,Se)$_2$ back contact to the surface. CZTS-surface precursors B and G have concentrations of Zn(S,Se) on and around the top surface of the grains. In samples C.7 and F.7, Zn(S,Se) forms at the front, in gaps between grains, and even near the back contact.

The effect of the various other annealing conditions on the morphology is shown in Fig. 3 for CZTSe-atop-CZTS precursors F(f) and Fig. 4 for CZTS-atop-CZTSe precursor G. Anneal 6 at maximum temperature 560 °C produces smaller and less laterally continuous grains than the 570 °C of anneal 7, but increasing the temperature to 580 °C for anneal 8 results in the formation of voids at the grain boundaries. In the case of precursor F, the high argon pressure of anneal 9 results in only slightly smaller grains than the lower pressure anneals, but for the precursor G (and for B and C, not pictured), recrystallization is incomplete and the grains are much smaller. For precursors F(f), anneals 10 and 11 at 35 kPa produce slightly larger grained
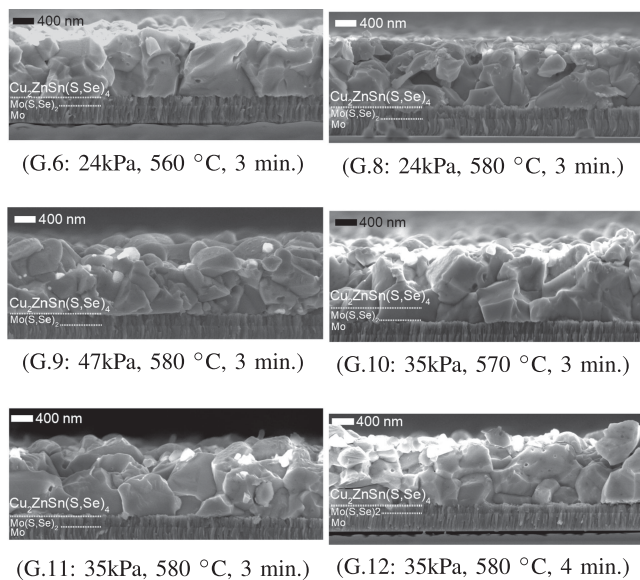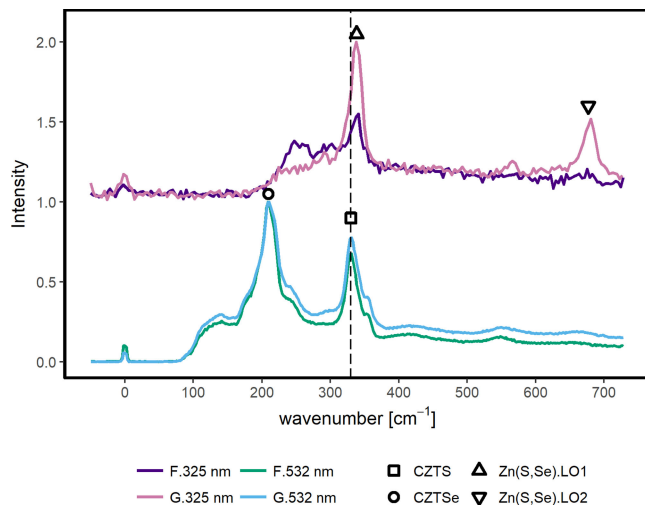

Fig. 5. Raman scattering spectra of 532 and 325 nm for samples F.7 and G.7. The dotted line at 330 cm^{-1} shows that the CZTS peak is present in both spectra. The 325 and 532 nm data have been separated on the vertical axis for clarity.

morphologies than anneals 6 and 7 at 24 kPa. For precursor G, anneals 10 and 11 are similar to 6 and 7, but the surface is slightly more rough, and the grains slightly smaller. Extending the 35 kPa anneal to 4 min as for Ff.12, and G.12 appears to produce a broader distribution of grain sizes, with both large and small grains present. Throughout the annealing series, CZTS-atop-CZTSe precursor G produces more flat CZTSSe surfaces than CZTSe-atop-CZTS precursor F.

We performed ZnS-resonant Raman spectroscopy with a 325-nm laser to characterize the S_r value for the Zn(S,Se) secondary phase [18] identified first by SEM-EDX. We also recorded the Raman spectrum with a 532-nm laser. These data are shown overlaid in Fig. 5 for samples F.7 and G.7. The Raman spectrum of sample B.7 was not significantly distinct from G.7,
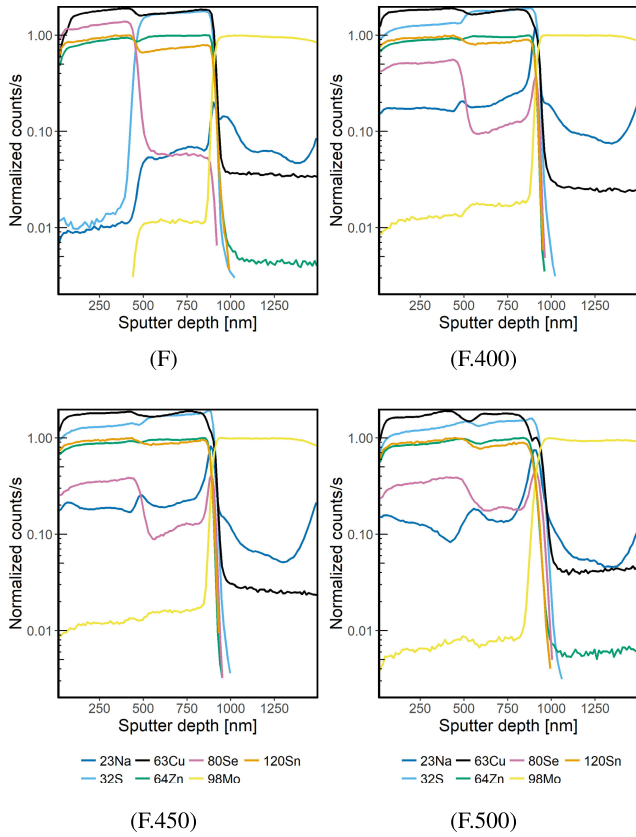
(F)

(F.400)

(F.450)

(F.500)

Fig. 6.   SIMS data for the precursor F bilayer ramp tests. Counts are normalized to fit a common scale. Data reprinted from [14].
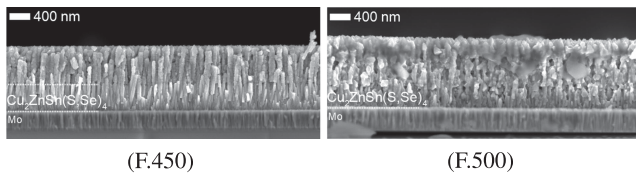

(F.450)

(F.500)

Fig. 7.   Cross-sectional SEM images for F.450 and F.500, showing the onset of crystallization. The dotted white line in the middle of the film for F.450 indicates the approximate position of the CZTS/CZTSe interface in the precursor. The contrast between the two layers is still clear at 450 °C. Reprinted from [14].

and the spectrum of C.7 not distinct from F.7, so B.7 and C.7 are omitted. Anneal 7 results are representative of all annealing results. In the 325-nm spectrum for annealed CZTS-atop-CZTSe sample G.7, the LO1 peak of Zn(S,Se) is at 338.5 cm^{-1}, and the LO2 peak at $\sim$677 cm^{-1}. The Zn(S,Se) LO1 peak shows a shoulder at 330 cm^{-1} which matches the CZTS peak from the 532-nm spectrum. The 325-nm spectrum for sample F.7 was weaker due to the lower surface concentration of Zn(S,Se), but otherwise showed the same details. These peak positions are consistent with the Zn(S,Se) secondary phase having an approximate [S]/([S]+[Se]) $\simeq$ 0.7 [18]. This is considerably more sulfur-rich than the absorber $S_r \simeq 0.4$ measured by EDX or GIXRD (see Fig. 9(a), later). That the Zn(S,Se) phase is considerably more S-rich than the absorber is consistent with the increases in the EDX sulfur to selenium signal ratio in the regions of line scans which intersect these grains (see Fig. 2, B.7 and F.7).
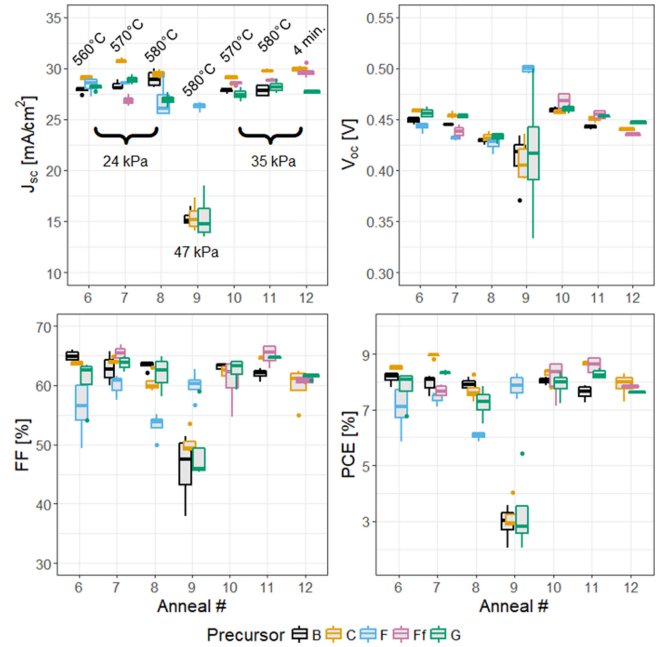

Fig. 8.   Device metadata from IV measurements. Key processing conditions are shown in the J_{sc} window for easy reference.
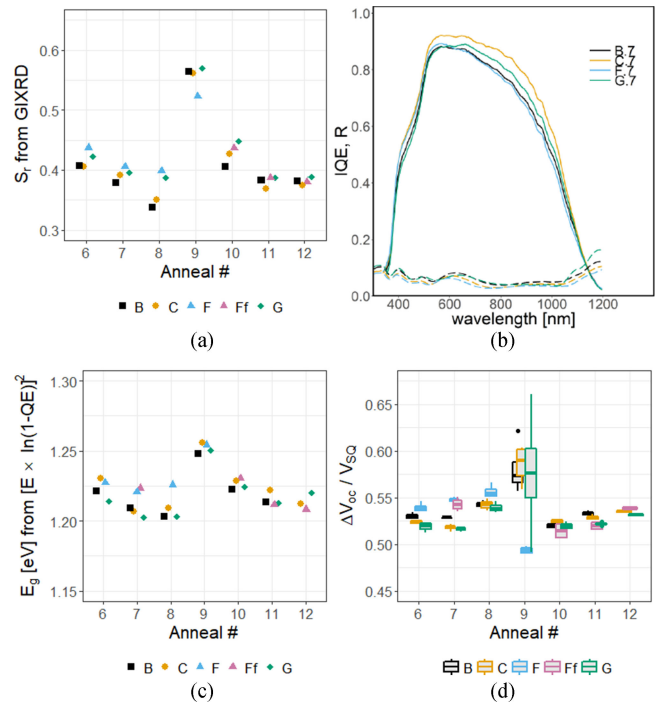
Fig. 9.   (a) Sulfur–selenium ratios S_r of the annealed absorbers, as estimated by GIXRD. (b) IQE for anneal 7 (solid lines) and device reflectivities R (dashed lines). (c) Bandgaps E_g estimated from QE $[E \times \ln(1 - QE)]^2$. (d) ΔV_{oc} deficit ratios calculated from QE (referencing the Shockley–Queisser voltage limit for a given E_g, V_{SQ}).

SIMS was used to investigate the elemental distribution during the ramp to temperature portion of the anneal. Bilayer precursors F were annealed under the same conditions as anneal 6, with the ramp to temperature truncated during the anneal by removal of the sample from the hot zone after it reached 400,

450, and 500 °C. We refer to these samples as F.400, F.450, and F.500, respectively. SIMS results are shown in Fig. 6, and the cross-sectional SEM for samples F.450 and F.500 is shown in Fig. 7. These results were first reported in a conference presentation, [14]. The sulfur–selenium step in the precursor F is partially removed by the displacement of selenium by sulfur at temperatures as low as 400 °C: less than half of the front-layer Se remains in the previously CZTSe portion of the precursor. At 400 °C, the back half shows a slightly elevated Se count and the S count in the front half of the film is much higher. The displacement of S by Se continues up to 500 °C. At 500 °C the sulfur step is essentially gone, and the Se count is rising in the back layer, likely due to the start of CZTSSe recrystallization near the back contact [11]. Grain growth is more advanced in the selenium rich front layer than the sulfur-rich back layer, for temperatures between 450 and 500 °C. It appears that most of the sulfur–selenium step present in the precursor is evened out during the ramp to annealing temperature in the tube furnace, leading to close-to-uniform S_r in the final annealed absorber.

SIMS further shows an accumulation of S and Se between the CZTSSe precursor layer and the Mo back contact even at 400 °C. This may indicate the formation of a thin Mo(S,Se)$_2$ back contact layer; such a layer is not yet thick enough to be seen clearly in the SEM cross section. The amount of Se accumulated at the back contact does not appear to change dramatically during the ramp to temperature. Sodium from the SLG is also seen to accumulate at the back contact at 400 °C. The sodium profile is relatively unchanged at 450 °C, but at 500 °C there is an apparent depletion of sodium in the middle of the film, where the CZTSe and CZTS layers of the precursor met. The comparison of absolute concentrations is difficult between the samples in SIMS, but it appears that as CZTSSe recrystallization advances in the front part of the selenium-rich layer, sodium migrates toward the front of the film but is not necessarily replaced by diffusion from the CZTS layer. This is consistent with the premise that sodium selenide helps facilitate recrystallization in CZTSSe [11].

Solar cell characteristics were extracted from IV measurements: the device metadata is shown in Fig. 8. Device B.12 was lost during cell scribing and is not included. Precursor Ff was additionally processed under anneal seven conditions to provide a reference for this similar precursor. Ff.7 has a lower current but higher fill factor than F.7, but otherwise they are quite similar, lending confidence that Ff is an appropriate substitute for F in anneals 10–12. Some of the trends that might be expected from the absorber morphologies shown in Figs. 1, 3, and 4 are immediately clear. Anneal 8 produces lower short-circuit currents, open-circuit voltages, and fill factors than anneal 7, correlating with the void formation seen from SEM. The J_{sc} and fill factor FF of sample B.8 are not reduced compared to B.7, but the SEM image (not included) for this sample does not show the same void formation as the other precursors. High pressure anneal 9 has generally low efficiency aside from larger grained sample F.9. Anneals 6–7 are very similar in quality to anneals 10–11, except for precursors F(f), for which higher pressure anneals 10–11 outperform anneals 6–7.

There are other noteworthy trends in the device data. Increasing the annealing temperature or time results in a reduction of V_{oc} for an increase in J_{sc}: this trend is present for 24 kPa anneals 6–8 and 35 kPa anneals 10–12. The absorber sulfur–selenium ratio S_r, as estimated from GIXRD peak shift, is shown in Fig. 9(a) and confirms that this tradeoff is the result of higher annealing temperatures leading to lower incorporation of sulfur compared to selenium, and thus to more narrow bandgaps. Bandgaps were estimated from external QE data and photon energy E using the $[E \times ln(1 - QE)]^2$ method and are shown in Fig. 9(c). The corresponding voltage deficit to Shockley–Queisser voltage limit ratio $\Delta V_{oc}/V_{SQ}$ is shown in Fig. 9(d). We note that this ratio compares V_{oc} not to E_g/q, but to the thermodynamic limit for open-circuit voltage at a given bandgap V_{SQ} [19]. For the comparison of anneals 7 to 6 (570 to 560 °C at 24 kPa) and 11 to 10 (580 to 570 °C at 35 kPa), the V_{oc} deficit generally decreases slightly for the selenium containing precursors. These data confirm that the loss of voltage with moderate increases in annealing temperature and time correspond only to a decreasing bandgap. For the hotter and longer anneals 8 and 12, there is a significant increase in voltage deficit which matches the lack of increase in J_{sc} with decreasing V_{oc} seen for the devices. Annealing conditions 8 and 12 produce substantially underperforming devices. The best devices come from moderate pressure anneals 7 (24 kPa, 570 °C) and 11 (35 kPa, 580 °C), for selenium containing precursors: C.7 ($J_{sc} = 30.7$ mA/cm^2; $V_{oc} = 0.451$ V; FF = 64.9%; PCE = 9.0%) and Ff.11 ($J_{sc} = 29.1$ mA/cm^2; $V_{oc} = 0.458$ V; FF = 66.5%; PCE = 8.9%).

We note that CZTSe precursor C generally produces high J_{sc} in annealed films, and that CZTS-surface precursors B and G generally yield lower J_{sc} values. Fig. 9(b) shows the internal quantum efficiency (IQE), IQE = QE/(1 − R) (solid lines), and reflectivity R (dashed lines). We previously noted that such differences might possibly be explained by reflectivity differences [14], but while CZTSe-surface precursors C and F process to devices with lower reflectivity, it is clear that the main contributor to the higher currents of all-selenium precursor C is electrical, not optical. The overall IQE for C.7 is significantly higher than for CZTSe-atop-CZTS precursor F. The large continuous grains of samples C.7 and G.7 also appear to correlate well with the superior long-wavelength collection of these samples compared to B.7 and F.7. If the slight sulfur–selenium gradients for precursors F(f) measured in EDX (see Fig. 2) were consistent across the device areas and represented in-grain differences, we would reasonably expect improved current collection from the resulting rear-grading of the bandgap [20], [21]. Since no such current improvements were observed, it is likely that the sulfur–selenium gradients result from incomplete recrystallization of the absorber.

IV. DISCUSSION

In this study, we have explored the deposition and annealing phase space for mixed sulfur–selenium anneals of a single ratio of elemental masses of sulfur and selenium, yielding annealed absorbers with sulfur–selenium ratios $S_r = [S]/([S] + [Se]) \simeq 0.4$. We annealed both CZTS and CZTSe precursors, as well as

bilayer stacked CZTSe-atop-CZTS (F(f)) and the reverse (G). In having performed mixed sulfur–selenium annealing of sulfur and selenium containing precursors, we have the opportunity to identify some of the ways in which selenide CZTSe and sulfide CZTS precursor material behave differently during thermal annealing in chalcogen atmosphere.

Sulfur–selenium steps sputtered into bilayer CZTSe/CZTS precursors are largely eliminated upon completion of annealing. In the CZTS-atop-CZTSe arrangement of precursor G, sulfur–selenium gradients inside CZTSSe grains were not detected. In the CZTSe-atop-CZTS bilayers F(f), such gradients were only ever very small of total change $\Delta S_r < 0.1$. F.7 shown in Fig. 2 showed the most extreme gradient of those found, and that device underperformed compared to most other anneal 7 samples. It is likely that these gradients in precursors F(f) reflect the more slow annealing process in that bilayer arrangement, and simply indicate that the absorber is not as fully recrystallized. The loss of the sulfur–selenium gradient is the result of the rapid influx of sulfur into the precursor during the ramp to the annealing temperature. At least for these compound cosputtered precursors, bilayer precursors of the thickness studied here do not provide a straightforward way of forming a sulfur–selenium bandgap grading in CZTSSe absorbers.

Raman spectroscopy showed the presence of solid solution ZnS_xSe_{1-x}, with $x \simeq 0.7$. SEM-EDX cross sections taken through the bright contrast grains seen in most of the SEM cross sections always showed a relative increase in Zn and S, and a drop in Se, Cu, and Sn, consistent with the sulfur-rich Zn(S,Se) composition estimated from resonant Raman. This was the case even for regions of absorbers formed from CZTSe precursor. One explanation for this composition is that the free energy of ZnS formation is significantly more negative than ZnSe formation [22]. Additionally, the Zn(S,Se) phase might nucleate during a time in the anneal when the partial pressure of sulfur is higher than selenium, as we describe later.

Zn(S,Se) formation during annealing was enhanced if the top surface of the precursor was a CZTS layer. ‘CZTS-atop-CZTSe’ precursor G in particular produced Zn(S,Se) almost exclusively at the top surface of its annealed films. If CZTS was not present at the surface, Zn(S,Se) formed randomly at grain boundaries and surfaces throughout the film. The implication is that zinc has some mobility during the annealing process, and that this mobility is different in CZTS and CZTSe regions. We will discuss this later, relating this mobility to the differential rates of recrystallization in different precursor materials.

In this study, we have observed by SEM and SIMS that regions of precursor with high selenium concentrations begin to recrystallize at lower temperatures than selenium poor, sulfur-rich regions. SIMS showed that CZTSe-rich regions take up sulfur from the annealing vapor at temperatures below 400 °C, but sulfur-rich regions do not selenize significantly until recrystallization takes place above 500 °C. We were able to obtain very large, laterally continuous CZTSSe grains from CZTSe containing precursors. We obtained relatively flat top surfaces by stacking CZTS precursor atop CZTSe, and these surfaces appeared more flat and had slightly higher reflectivity than those annealed from CZTS-only precursors. It is known from *in situ*
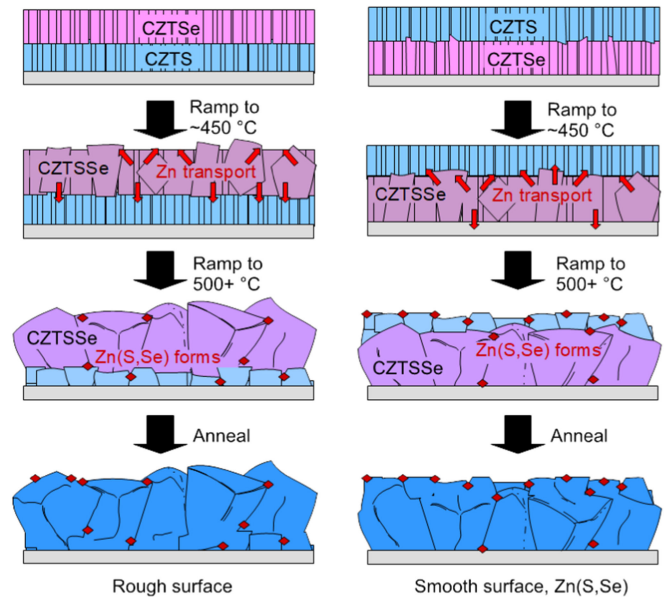

Fig. 10. Diagrammatic representation of a simple model for absorber growth in mixed sulfur–selenium anneals of compound-sputtered CZTS/CZTSe multilayer precursors. The growing CZTSSe becomes more sulfur-rich as the reaction proceeds, indicated by the changing shade of the grains. The length scales of conjectured cation transport during the annealing process are unknown, and not represented to scale.

XRD measurements that selenization occurs at lower temperature than sulfurization [23]. Our study shows that the presence of selenium in the precursor itself enhances the rate of recrystallization at a given temperature—or equivalently, time during an anneal requiring a ramp to target temperature. For any 'snapshot' of the annealing process, there can be a differential degree of recrystallization when comparing different locations in the absorber, based on the chalcogen content of those locations.

The orientation of the fine-grain layer in annealed solution-deposited CZTSSe is known to be controllable by the introduction of elemental selenium layers, and this control is rationalized by a model of selenium and copper selenide liquid-phase-assisted grain growth [24]. Tin [25] and sodium selenide [11], [26] liquid phases have been implicated in the enhancement of crystal growth rate in CZTSSe. Pulling these threads together with the results of this study, we propose a basic model for the crystal sintering and growth of compound-sputtered CZTS/CZTSe multilayers, shown diagrammatically in Fig. 10.

In this model for the selenium-rich mixed sulfur–selenium anneal, the CZTSe portions of the precursor become partially sulfurized at or below 400 °C, but retain high concentrations of selenium. Liquid selenide phases or selenium-rich regions which otherwise have higher coefficients of diffusion than sulfur-rich regions facilitate growth from around 450 °C in these CZTSe regions. The cubic CZTSSe precursor [27] recrystallizes and sinters into single-phase kesterite CZTSSe, with some capacity for excess cation transport through the growing crystal. This transport may be through a liquid flux, or simply diffusion driven by the growing crystal interfaces. Excess Zn can be transported some distance before nucleating Zn(S,Se), with the sulfur provided either from the now sulfurized CZTSSe precursor or

directly from the gas phase. In the absence of a CZTS layer in the precursor, the Zn(S,Se) nucleates at surfaces throughout the growing film, including grain boundaries, at a time when sulfur is still plentiful in the anneal. This leads to sulfur-rich ZnS$_{0.7}$Se$_{0.3}$.

If a CZTS precursor layer is present, that layer begins recrystallization after the temperature increases beyond 500 °C, corresponding to a later time in the ramped tube furnace anneal. The grain structure of the neighboring selenide rich region is more established and cannot take up or provide nucleation sites for Zn(S,Se), so any excess zinc compared to the single-phase stoichiometry remains localized around the sulfide layer region. We speculate that nucleation of Zn(S,Se) at the upper free surface is less constrained than at other grain boundaries, and thus, statistically more common. This leads to the high density of surface Zn(S,Se) for annealed 'surface CZTS' precursors. Since the CZTS layer grows for a shorter period of time, grains are smaller in this region in the early stages of the anneal. The CZTSe region grows faster and larger in the early stages of the anneal. Later in time, during the high temperature stage of the anneal, these grains might sinter together or continue recrystallizing under tighter spatial restrictions from neighboring grains. For bilayer precursors with an upper CZTS layer and a lower CZTSe layer, the smaller upper surface grains coalesce into a more flat surface, while the opposite stacking orientation leads to a rough surface.

In order to rationalize the trends for morphology as seen by SEM and the device trends from Figs. 8 and 9, we need some model for elemental chalcogen availability during annealing. The trends we have observed are: that an extremely high background argon pressure results in incomplete recrystallization and far-from-optimum devices; that anneals beyond a certain temperature limit or time limit result in the formation of smaller grains and sometimes voids, resulting in more poor performance; and that moderate background argon pressures produce more complete recrystallization, yielding better devices. We postulate that the mixed sulfur–selenium annealing is characterized by a sulfur-rich phase during the ramp and the start of the anneal, a more evenly mixed S-Se atmosphere through the first 3 min of the anneal, and a potentially sulfur-poor phase at times near and longer than 3 min.

The model for the mixed annealing is shown diagrammatically in Fig. 11, for a maximum annealing temperature of 580 °C, and for background argon pressures of 24, 35, and 47 kPa. This diagram thus represents anneals 8, 11, and 9, respectively, but we will discuss also how the more successful anneal 7 at 570 °C fits into the description. Time and temperature are related via the ramping rate of the sample when it is pushed into the hot zone: we show only the period from near the end of the ramp, for temperatures ~ 500 °C and higher. The maximum partial pressures of sulfur and selenium are represented accurately, but the rate of pressure increase and loss depends on the specifics of the annealing setup, and has not been measured explicitly. The gradients of the partial pressures are only intended to be illustrative, not absolute. Likewise, the boundaries between the sulfur partial pressure regimes described are not known, and those shown are merely representative.
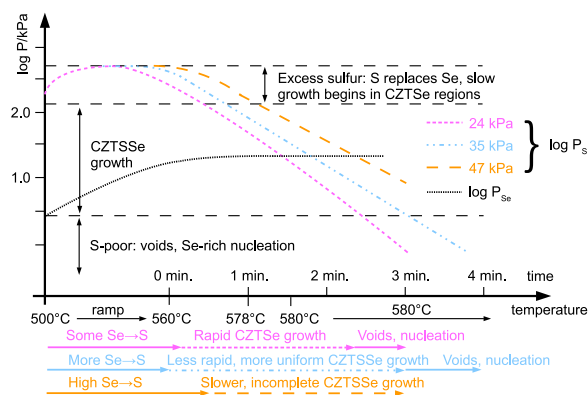

Fig. 11. Simple model for the evolution of chalcogen partial pressures during mixed sulfur–selenium annealing of CZTSSe precursors. The rates of increase and decay of chalcogen partial pressures are qualitative, as they could not be measured directly. The three colored lines represent the partial pressure of sulfur P_S at the three different argon background pressures. The fine black dotted line represents the partial pressure of selenium, P_{Se}.

At 500 °C, the sulfur vapor pressure is $\log_{10}(P_S/\text{kPa}) \simeq 2.3$, rising to 2.6 by 560 °C [28]. In this "excess sulfur" region of the anneal, S is able to displace precursor Se. Since only a small mass of sulfur exists, and the partial pressure is very high, sulfur loss from the graphite box depletes the sulfur supply quickly [13]. Higher background argon pressures extend the period of time for which the anneal is sulfur-rich [29], pushing more sulfur into the precursors. Recrystallization is already occurring during the ramp and the sulfur-rich part of the anneal, but we postulate that it is slower for more sulfur-rich precursors, based on our SIMS results. We postulate that the sulfur-rich ZnS$_{0.7}$Se$_{0.3}$ secondary phase forms during or just after this high sulfur partial pressure time period.

After most of the elemental sulfur is consumed, the sulfur partial pressure in the box falls. The selenium partial pressure rises during the ramp and maintains near $\log_{10}(P_S/\text{kPa}) \simeq 1.3$ [30]. It is possible that in the later stages of the anneal, especially for the lowest argon pressure anneal (24 kPa), the selenium is also expended and the partial pressure drops. However, in order to understand our results it is not necessary to verify this possibility. When P_S and P_{Se} become comparable in the middle stages of the anneal (~ 30 s–3 min), the chalcogen gas mix encourages rapid recrystallization of $S_r \sim 0.4-0.6$ CZTSSe. The higher the background partial pressure, the slower the sulfur loss. This has two effects: first there is less early selenium incorporation in the sample, slowing crystal growth; second, it takes longer for the "ideal" partial pressure ratio to be achieved, also slowing growth. This explains the morphology and device results from anneal 9 (580 °C, 47 kPa): The anneal is too sulfur-rich to be complete in the 3–4 min before the sulfur-poor condition leads to tin and sulfur loss [13]. The growth is slowed, resulting in small sulfur-rich grains at the end of the short annealing process. The consequence might be enhanced recombination and/or band bending at grain boundaries, leading to the high voltage deficits and low currents observed. For 35 kPa anneal 11, a good balance is struck between sulfur enrichment in the early stages of growth and sulfur loss during the later stages of growth, leading to a partial pressure profile that lies in the 'ideal'

band for the duration of the 3 min anneal. The recrystallization is well advanced, leading to large grains, lower recombination, and better collection. We note that for anneal 7 at 24 kPa and 570 °C (not depicted), the lower maximum temperature probably puts the sulfur partial pressure loss along a similar path, with a lower peak P_S, and likewise to good quality grains. In both cases, the devices which result are higher in quality than the other conditions.

This model of changing chalcogen relative partial pressures might help explain why precursor G produces less flat morphologies in the 35 kPa anneals 10 and 11 than the 24 kPa anneals 6–8. For the higher background pressure, more selenium is displaced during the sulfur-rich initial phase of the annealing. The differential between growth rates of the two layers is reduced as a consequence of the reduction in selenium concentration, reducing the flattening effect. For the opposite bilayer arrangement of precursor F(f), the 35 kPa condition produces more uniformly annealed absorber layers and higher performing devices than the 24 kPa condition. We are unable to explain this fully, but postulate that the slower rate of growth of the sulfide-like back half of the film might place some limits of the diffusion of sodium from the glass, leading to a wider distribution of crystal quality. We would need to perform detailed SIMS comparisons of the two bilayer arrangements to confirm this hypothesis, but have not yet had the opportunity to do so.

The sulfur loss and potential selenium loss at later times in the anneal imposes a practical limit on how far the anneal can progress. This is the case for the 24 kPa, 580 °C anneal 8 depicted. Here, the sulfur source is quickly exhausted because of the high anneal temperature and low background pressure: sulfur escapes more quickly from the annealing box. Initial recrystallization is more rapid due to the lower concentration of sulfur forced into the precursor, but the anneal quickly runs out of sulfur. The result might be nucleation and growth of more selenium rich-CZTSSe grains, at the expense of established grains [17], [31]. The kinetic enhancement of selenization by sulfur removal [32] might aid in this selenium-rich nucleation. If the selenium source is also exhausted, the formation of voids by decomposition of the CZTSSe could only be expected to increase. A similar scenario would play out for the 4 min anneal 12: the sulfur runs out, with subsequent renucleation of selenium-rich grains, lowering the average grain size. Tin loss might also lead to an increase in deep defect formation [13]. In both cases, higher voltage deficits and lower currents could be expected, and this is what was observed.

V. Conclusion

The value of selenium inclusion in CZTSSe precursors is in increasing the rate of recrystallization during annealing for any given set of annealing conditions. CZTSe precursor layers show significantly more advanced recrystallization at 500 °C than CZTS layers, resulting in better grain growth in the allowable 3 min experimental window. In our current tube furnace annealing setup, this allowable time window is defined primarily by chalcogen loss from the annealing box, but other time restrictions, such as limited sodium diffusion or excessive Mo(S,Se)$_2$

formation, may apply for different annealing arrangements. The large, continuous grains which grow from selenium containing precursor layers result in lower recombination and better collection, and thus, to higher solar cell performance. Because of this enhanced growth, including selenium in the precursor allows us to achieve relatively higher quality devices, even in a restricted annealing phase space.

The device quality is modest overall, with highest performance 9.0% PCE (no antireflective coating), with much room for improvement compared to record devices. We believe the primary restrictions on our device quality result from the chalcogen atmosphere loss described earlier. This chalcogen loss must therefore be addressed or worked around to significantly improve the quality of the bulk absorber. While we are not able to preserve sulfur–selenium gradients for bandgap grading engineering, we are able to exercise some measure of control over the roughness of the surface and the spatial distribution of the secondary phase Zn(S,Se) by stacking the CZTSe and CZTS of the precursor appropriately. In particular, CZTS top layers with a CZTSe underlayer result in smooth surface absorbers with Zn(S,Se) confined almost exclusively to the top surface of the absorber. We are still exploring the possibilities of precursor growth engineering using sulfur–selenium steps and gradients, and believe that further enhancements in performance are possible using this approach.

References

[1] W. Wang et al., "Device characteristics of CZTSSe thin-film solar cells with 12.6% efficiency," Adv. Energy Mater., vol. 4, 2014, Art. no. 1301465.

[2] T. Todorov, H. Sugimoto, P. Gunawan, T. Gokmen, and D. B. Mitzi, "High-efficiency devices with pure solution-processed Cu$_2$ZnSn(S,Se)$_4$ absorbers," IEEE J. Photovolt., vol. 4, no. 1, pp. 483–485, Jan. 2014.

[3] D. A. R. Barkhouse, O. Gunawan, T. Gokmen, T. Todorov, and D. B. Mitzi, "Device characteristics of a 10.1% hydrazine-processed Cu$_2$ZnSn(S,Se)$_4$ solar cell," Prog. Photvolt., Res. Appl., vol. 20, pp. 6–11, 2012.

[4] S. G. Haass et al., "11.2% efficient solution processed kesterite solar cell with a low voltage deficit," Adv. Energy Mater., vol. 5, 2015, Art. no. 1500712.

[5] K. Yang et al., "A band-gap-graded CZTSSe solar cell with 12.3% efficiency," J. Mater. Chem. A, vol. 4, pp. 10151–10158, 2016.

[6] R. Bodeux, F. Mollica, and S. Delbos, "Growth of Cu$_2$ZnSnSe$_4$ by cosputtering and reactive annealing atmosphere," Sol. Energy Mater. Sol. Cell., vol. 132, pp. 67–73, 2015.

[7] C. Platzer-Björkman, J. J. Scragg, H. Flammersberger, T. Kubart, and M. Edoff, "Influence of precursor sulfur content on film formation and compositional changes in Cu$_2$ZnSnS$_4$ films and solar cells," Sol. Energy Mater. Sol. Cell., vol. 98, pp. 110–117, 2012.

[8] R. Sun et al., "Cu$_2$ZnSnSSe$_4$ solar cells with 9.6% efficiency via selenizing Cu-Zn-Sn-S precursor sputtered from a quaternary target," Sol. Energy Mater. Sol. Cell., vol. 174, pp. 42–49, 2018.

[9] R. Sun et al., "High-sulfur Cu$_2$ZnSn(S,Se)$_4$ films by sulfurizing as-deposited CZTSe film: The evolutions of phase, crystallinity and S/(S+Se) ratio," J. Alloys Compounds, vol. 695, pp. 3139–3145, 2017.

[10] D. Hwang et al., "Single-step sulfo-selenization method for achieving low open circuit voltage deficit with band gap front-graded Cu$_2$ZnSn(S,Se)$_4$ thin films," Sol. Energy Mater. Sol. Cell., vol. 161, pp. 162–169, 2017.

[11] N. Ross, J. K. Larsen, S. Grini, L. Vines, and C. Platzer-Björkman, "Practical limitations to selenium annealing of compound co-sputtered Cu_2ZnSnS_4 as a route to achieving sulfur-selenium graded solar cell absorbers," *Thin Solid Films*, vol. 623, pp. 110–115, 2017.

[12] T. Ericson, T. Kubart, J. J. Scragg, and C. Platzer-Björkman, "Reactive sputtering of precursors for Cu_2ZnSnS_4 solar cells," *Thin Solid Films*, vol. 520, pp. 7093–7099, 2012.

[13] Y. Ren *et al.*, "Evolution of Cu_2ZnSnS_4 during non-equilibrium annealing with quasi-in situ monitoring of sulfur partial pressure," *Chem. Mater.*, vol. 29, no. 8, pp. 3713–3722, 2017.

[14] N. Ross, S. Grini, L. Vines, and C. Platzer-Björkman, "Mixed sulfur and selenium annealing study of compound-sputtered $Cu_2ZnSnS_4/Cu_2ZnSnSe_4$ precursors," *Proc. IEEE Photovolt. Spec. Conf.*, vol. 44, 2017.

[15] J. Larsen *et al.*, "Surface modification through air annealing $Cu_2ZnSn(S,Se)_4$ absorbers," *Thin Solid Films*, vol. 633, pp. 118–121, 2017.

[16] D. M. Berg *et al.*, "Discrimination and detection limits of secondary phases in Cu_2ZnSnS_4 using X-ray diffraction and Raman spectroscopy," *Thin Solid Films*, vol. 31, pp. 113–123, 2014.

[17] S. Grini *et al.*, "Secondary ion mass spectrometry as a tool to study selenium gradient in $Cu_2ZnSn(S,Se)_4$," *Physica Status Solidi C*, vol. 14, 2017, Art. no. 1600187.

[18] M. Dimitrievska *et al.*, "Resonant Raman scattering of ZnS_xSe_{1-x} solid solutions: The role of S and Se electronic states," *Phys. Chem. Chem. Phys.*, vol. 18, pp. 7632–7640, 2016.

[19] S. Rühle, "Tabulated values of the Shockley–Queisser limit for single junction solar cells," *Sol. Energy*, vol. 130, pp. 139–147, 2016.

[20] T. Kato, N. Sakai, and H. Sugimoto, "Efficiency improvement of $Cu_2ZnSn(S,Se)_4$ submodule with graded bandgap and reduced backside ZnS segregation," *Proc. 40th IEEE Photovolt. Spec. Conf.*, 2014, vol. 41, pp. 0844–0846.

[21] C. Li *et al.*, "Impact of sequential annealing step on the performance of $Cu_2ZnSn(S,Se)_4$ thin film solar cells," *Superlattices Microstruct.*, vol. 95, pp. 149–158, 2016.

[22] A. Nasar and M. Shamsuddin, "Investigations of the thermodynamic properties of zinc chalcogenides," *Thermochimica Acta*, vol. 205, pp. 157–169, 1992.

[23] M. H. Sayed *et al.*, "*In situ* XRD investigation of re-crystallization and selenization of CZTS nanoparticles," *J. Alloys Compound*, vol. 686, pp. 24–29, 2016.

[24] C. J. Hages, M. J. Koeper, C. K. Miskin, K. W. Brew, and R. Agrawal, "Controlled grain growth for high performance nanoparticle-based kesterite solar cells," *Chem. Mater.*, vol. 28, pp. 7703–7714, 2016.

[25] J. Li *et al.*, "Growth of $Cu_2ZnSnSe_4$ film under controllable Se vapor composition and impact of low Cu content on solar cell efficiency," *ACS Appl. Mater. Interfaces*, vol. 8, pp. 10 283–10 292, 2016.

[26] C. M. Sutter-Fella *et al.*, "Sodium assisted sintering of chalcogenides and its application to solution processed $Cu_2ZnSn(S,Se)_4$ thin film solar cells," *Chem. Mater.*, vol. 26, pp. 1420–1425, 2014.

[27] T. Ericson, J. J. Scragg, T. Kubart, T. Törndahl, and C. Platzer-Björkman, "Annealing behavior of reactively sputtered precursor films for Cu_2ZnSnS_4 solar cells," *Thin Solid Films*, vol. 535, pp. 22–26, 2013.

[28] D. Peng and J. Zhao, "Representation of the vapour pressures of sulfur," *J. Chem. Thermodyn.*, vol. 33, pp. 1121–1131, 2001.

[29] J. J. Scragg, "Studies of Cu_2ZnSnS_4 films prepared by sulfurisation of electrodeposited precursors," Ph.D. dissertation, Univ. Bath, Bath, U.K., 2010.

[30] A. M. Klimova, V. A. Anaichev, M. Arif, and L. N. Blinov, "Investigation of the saturated vapor pressure of zinc, selenium, and zinc selenide," *Glass Phys. Chem.*, vol. 31, pp. 760–762, 2005.

[31] N. Ross *et al.*, "$Cu_2ZnSn(S,Se)_4$ solar cell absorbers from diffusion of selenium into annealed Cu_2ZnSnS_4 absorbers," *Proc. IEEE 43rd Photovolt. Spec. Conf.*, 2016, vol. 43, pp. 0492–0497.

[32] G. Chen *et al.*, "Influence of selenization atmosphere on the $Cu_2ZnSn(S,Se)_4$ thin films and its correlation to the performance of solar cells," *Mater. Res. Bull.*, vol. 94, pp. 164–169, 2017.

Authors' photographs and biographies not available at the time of publication.